ACS APPLIED MATERIALS & INTERFACES
Research Article
www.acsami.org

Ferroelectric Tunnel Junction for Dense Cross-Point Arrays

Hong-Sub Lee,[†] Wooje Han,[†] Hee-Yoon Chung,[†] Marcelo Rozenberg,[‡,§] Kangsik Kim,[∥] Zonghoon Lee,[∥] Geun Young Yeom,[⊥] and Hyung-Ho Park[*,†]

[†]Department of Materials Science and Engineering, Yonsei University, Seodaemun-Ku, Seoul 120-749, Korea

[‡]Laboratoire de Physique des Solides, CNRS-UMR 8502 Université Paris-Sud, Orsay 91405, France

[§]IFIBA-Conicet and Departamento de Física, FCEN, Universidad de Buenos Aires, Ciudad Universitaria Pabellón I, (1428) Buenos Aires, Argentina

[∥]School of Materials Science and Engineering, Ulsan National Institute of Science and Technology (UNIST), Ulsan 689-798, Korea

[⊥]Department of Advanced Materials Science and Engineering and SKKU Advanced Institute of Nanotechnology, Sungkyunkwan University, Suwon, Kyunggi-do 440-746, Republic of Korea

Supporting Information

ABSTRACT: Cross-point array (CPA) structure memories using a memristor are attracting a great deal of attention due to their high density integration with a $4F^2$ cell. However, a common significant drawback of the CPA configuration is crosstalk between cells. To date, the CPA structure using a redox-based memristor has restrictions to minimize the operating current level due to their resistive switching mechanism. This study demonstrates suitable characteristics of a ferroelectric tunnel junction (FTJ) for the memristor of the CPA structure using an electrostatic model. From the FTJ of the Au/*p*-type $Pr_{0.98}Ca_{0.02}MnO_3$ (4 nm)/ $BaTiO_3$ (4.3 nm)/*n*-type $Ca_{0.98}Pr_{0.02}MnO_3$ (3 nm)/ Pt(111) structure, which has a higher and thicker potential barrier, a good memristive effect for the CPA structure with a high nonlinear current−voltage curve and low current operation, was obtained by Δ Fowler−Nordheim tunneling with effectively blocked direct tunneling and thermionic emission. The FTJ demonstrated reduced sneak current and the possible for high nonlinearity.

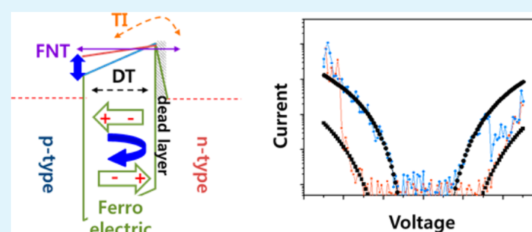

KEYWORDS: *ferroelectric tunnel junction, cross point array structure, memristor, sneak current, perovskite manganite family*

1. INTRODUCTION

Next-generation nonvolatile memory (NVM) with high density, low power consumption, fast speed, and nonvolatile characteristics is required to overcome restrictions of dynamic random access memory (RAM) and flash memory. The present strong candidates for NVMs are ferroelectric RAM, phase change RAM, magnetic RAM, and resistive RAM that use the state change of materials described in their names, not a current charge trap method.[1−7] Therefore, the materials are key to realizing NVM. The other side, a cross-point array (CPA) structure using a memristor also has attracted great deal of attention as much as material characteristics due to its high density integration with a $4F^2$ cell because each cell in the CPA structure is operated by only a word line and a bit line without a selection transistor.[8−10] However, a common significant drawback of the CPA configuration is the issue of crosstalk between cells. As shown in Figure 1a, the "read" and "write" operation of the resistive RAM (ReRAM) in a CPA configuration is performed by commuting a cell at the crossing point between a "word" and a "bit" line. The crosstalk problem may occur when reading and writing a cell in a high resistance state (HRS), which is surrounded by cells in the low resistance state (LRS). When the read and write operation occurs, the unselected cells that are sharing the word and bit lines with a selected cell receive half of the read and write voltage. Therefore, a "sneak current" flowing through the adjacent cells, as shown in current path B (green line), may reduce the readout margin and induce reading errors. Additionally, a "voltage drop" is induced in the writing operation. As shown in Figure 1b, an increase of the number of word lines "*N*" increases the sneak current due to the parallel contact between selected and unselected cells. These issues lead to a reduction of the cell density in cross-point arrays, and represent one of the main bottlenecks for actual implementation of these systems. In order to overcome these issues, ReRAM studies designed a solution as the nonlinearity current−voltage (*I*−*V*) curve, which reduces the current density at half of the operating voltage through an additional potential barrier stack and the higher nonlinear curve can achieve a larger number of "*N*". Therefore, the low current level and high nonlinearity may be an important competitiveness index for the CPA structure with a high density NVM. However, redox-based memristors are restricted to minimize the sneak current because they require larger current level than a certain quantity for resistive

Received: July 8, 2015
Accepted: September 17, 2015
Published: September 17, 2015

ACS Publications © 2015 American Chemical Society

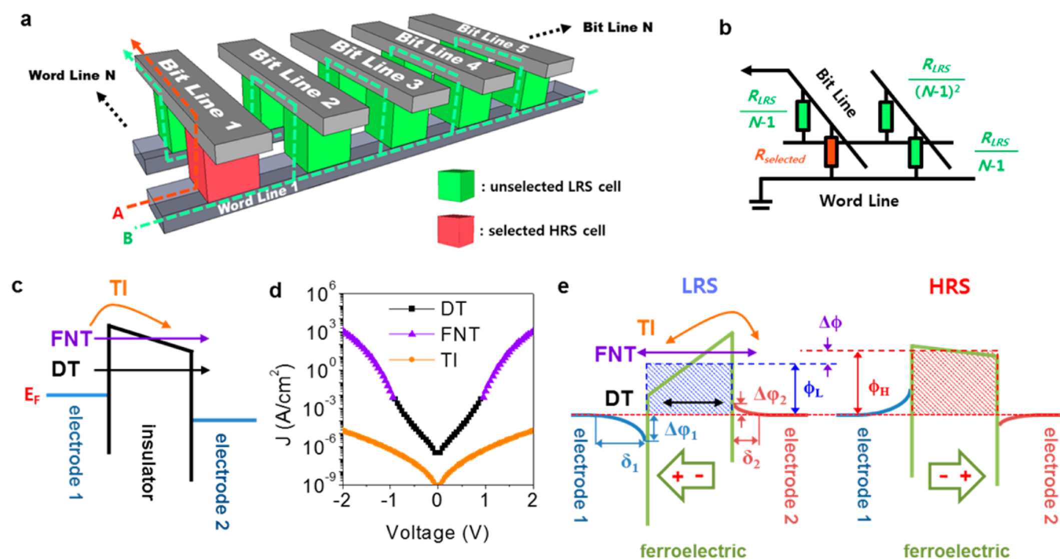

Figure 1. A cross-point array configuration and ferroelectric tunnel junction. (a) Schematic diagrams of the cross-talk in a cross-point array configuration of a selected HRS cell surrounded by unselected LRS cells and (b) cross-point array circuit (N × N). (c) A schematic of the band diagram and carrier transport mechanisms such as J_{DT}, J_{FNT}, and J_{TI} in the metal/insulator/metal structure. (d) *I*−*V* curves of J_{DT}, J_{FNT}, and J_{TI} (the parameters were $d = 3.2$ nm, $\varphi_{B,1} = \varphi_{B,2} = 1$ eV, $m_{e,ox} = m_e$, $\varepsilon_{ifl} = 10$, $A^{**} = 10^6$ $Am^{2-}K^{-2}$, and $T = 300$ K). (e) A schematic of the electrostatic model for the memristive effect mechanism in FTJ (the band diagram was aligned to the Fermi level).

switching by electrochemical migration and/or redox.[5,11,12] Therefore, this study focused on the application of the memristive effect of the ferroelectric tunnel junction (FTJ) to the CPA structure for minimization of the sneak current. The memristive effect of FTJ achieves resistive switching characteristic by the direction of ferroelectric polarization. In this case, the memristive effect could be obtained regardless of the current level. Therefore, it permits resistive switching operation in such conditions as a very low current level, low power consumption, and minimized voltage drop in the CPA structure.

Figure 1c is the schematic simple band diagram when a negative bias was applied to electrode 1, indicates three carrier transport mechanisms from electrode 1 to 2 in the electrode 1/insulator/electrode 2 structure. In general, the mechanisms considered by direct tunneling (DT), Fowler−Nordheim tunneling (FNT), thermionic emission (TI) (for more details, see Section A in the Supporting Information).[13−16] Figure 1d shows *I*−*V* curves of J_{DT}, J_{FNT}, and J_{TI} based on the Section A in Supporting Information. When temperature T is fixed, J_{DT}, J_{FNT}, and J_{TI} depend on the thickness and height of the potential barrier. Therefore, in the appropriately higher and thicker potential barrier, a high nonlinear *I*−*V* curve by J_{FNT} with minimized J_{DT} and J_{TI} can be obtained. Additionally, if a ferroelectric material is applied to the barrier, the FTJ memristive effect of the high nonlinear *I*−*V* curve can be achieved by an electrostatic effect (a change in the potential barrier height). Recently, Lee et al.[11] reported a very high nonlinear resistive switching curve using a redox-based memristor that was obtained from an additional crested barrier with J_{FNT}. A memristive effect of FTJ shows a change in the tunneling current according to their direction of remnant polarization. Following the mechanism studies, the electrostatic effect shown in Figure 1e is primarily used to explain the tunnel electroresistance (TER) effect.[1,17−22] Figure 1e shows a schematic band diagram of the electrostatic effect of FTJ. An electrode 1/ferroelectric/electrode 2 structure was fabricated using different electrode materials such that each electrode had a different work function ($\Phi_1 < \Phi_2$) and Thomas−Fermi screening length ($\delta_1 > \delta_2$). The electrostatic effect originated from the different screening in each electrode side as $\delta_1 > \delta_2$. In this structure, incomplete screening at the two interfaces of the electrode 1/ferroelectric/electrode 2 structure induced $\Delta\varphi_1$ and $\Delta\varphi_2$, in which $\Delta\varphi_1$ was larger than $\Delta\varphi_2$ because $\delta_1 > \delta_2$. Therefore, in the case of $\Delta\varphi_1 > \Delta\varphi_2$, the mean barrier height ϕ ($\phi = (\varphi_1 + \varphi_2)/2$) with the depolarizing field changed according to the polarization direction (up and down) of the ferroelectric layer. With this change, the memristive effect was obtained by inducing a different tunneling current. Therefore, a different electrode on the top and bottom is the most important role, and many studies fabricated a asymmetric electrode using a small doped semiconductor and metal.

On the basis of Section A in the Supporting Information, J_{TI} strongly depends on the barrier height, and ϕ should be at least larger than 1 eV in both high and low barrier states to effectively suppress J_{TI}. Therefore, this study fabricated FTJ as an oxide semiconductor/ferroelectric/oxide semiconductor structure to avoid the degradation effect of the barrier height as Schottky pinning in which the oxide semiconductor electrode was a *p*-type semiconductor $Pr_{0.98}Ca_{0.02}MnO_3$ (PMO) for the top and an *n*-type semiconductor $Ca_{0.98}Pr_{0.02}MnO_3$ (CMO) for the bottom of the perovskite Manganite family as $RE^{3+}_{1-x}AE^{2+}_{x}MnO_3$ (RE: rare earth AE: alkaline earth). The PMO and CMO of this study were a hole-doped Mott insulator and an electron-doped band insulator (for more details, see Section B in Supporting Information).[23−25] In this case, PMO has a high resistance characteristic via a strongly localized hole carrier on their carrier transport mechanism as the double exchange model while CMO has a delocalized electron carrier.[25−30] And the screening effect by a ferroelectric dead layer at bottom interface could be considered in which the dead layer is generally formed at the bottom by interdiffusion, lattice mismatch, or interface defects in the crystal growth process.[31−34] $BaTiO_3$ typically used for FTJ, was adopted to the ferroelectric layer. Consequently, as shown in Figure 2a, the multilayer device as Au/

DOI: 10.1021/acsami.5b06117
ACS Appl. Mater. Interfaces 2015, 7, 22348−22354

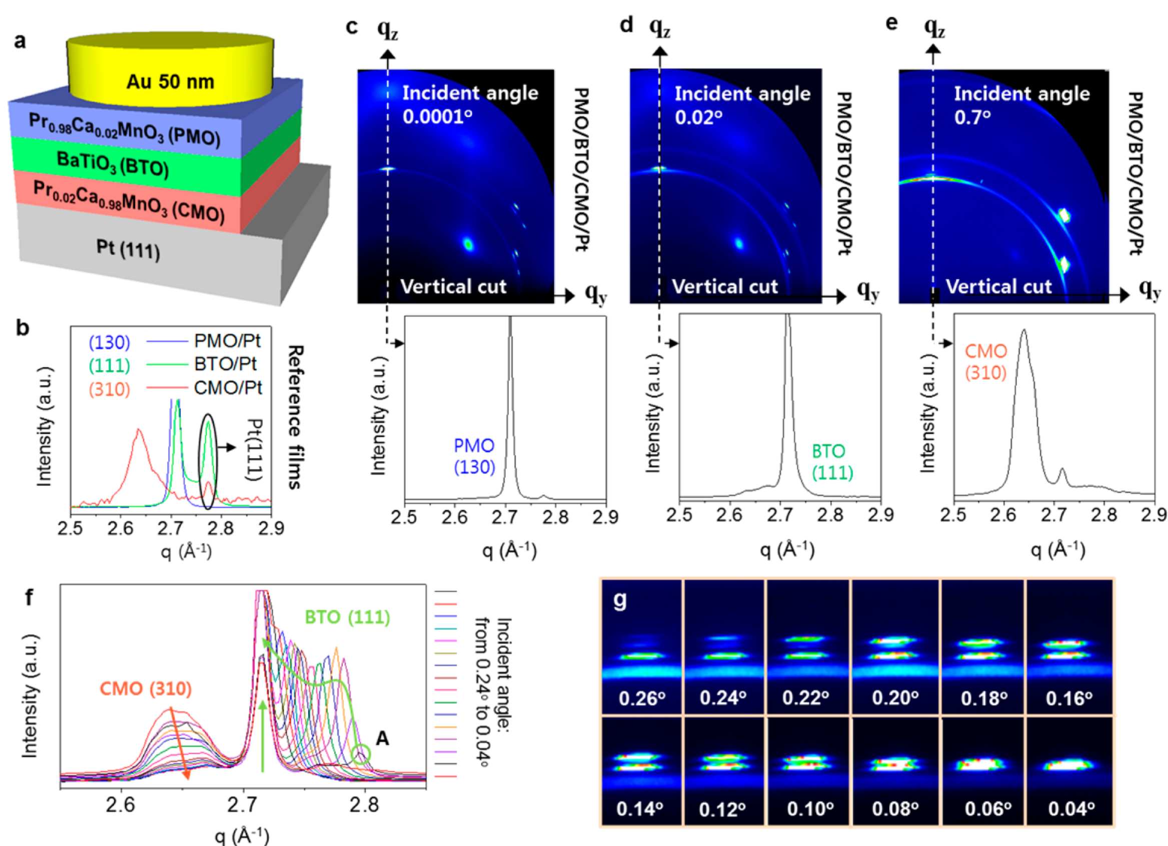

Figure 2. FTJ device structure. (a) Schematic diagram of the Au/PMO (4 nm)/BTO (4.3 nm)/CMO (3 nm)/Pt(111) structure. (b) GI-WAXD patterns of the 1D diffraction intensity curves of PMO/Pt(111), BTO/Pt(111), and CMO/Pt(111) reference films. GI-WAXD patterns of the 2D image with 1D diffraction intensity curves (vertical cut) of the Au/PMO (4 nm)/BTO (4.3 nm)/CMO (3 nm)/Pt(111) structure according to various incident angles such as (c) 0.0001, (d) 0.02, and (e) 0.7°. For 2D intensity distribution, the horizontal (or out-of-plane) component of the scattering vector q_y is plotted along the x axis, and the vertical (or in-plane) component of the scattering vector q_z is plotted along the y axis. The observed diffraction peaks are addressed according to Miller indices (hkl). (f) 1D diffraction intensity curves and (g) 2D image at the corresponding angle to the BTO/CMO interface region (from 0.26 to 0.04°, interval: 0.02°).

$Pr_{0.98}Ca_{0.02}MnO_3/BaTiO_3/Ca_{0.98}Pr_{0.02}MnO_3/Pt(111)$ was fabricated for the CPA structure using J_{FNT} by $\Delta\phi$. Novel metals of Au and Pt were used as the top and bottom electrode to prevent redox at the top and bottom.

2. EXPERIMENTAL SECTION

A three-layer [PMO (4 nm)/BTO (4.3 nm)/CMO (3 nm)] film was successively fabricated by rf magnetron sputtering (in situ) on a chemically cleaned $Pt(111)/Ti/SiO_2/Si$ substrate. The background pressure in the sputter chamber was less than 1.0×10^{-7} Torr, and the deposition conditions of the power, substrate temperature, deposition pressure and deposition rate were 100 W, 550 °C, 2 mTorr, and 1 nm/min, respectively ($Ar::O_2$ ratios of sputtering gas were 4::1 and 4::0, respectively). After the film fabrication, a circular electrode of Au (50 nm) was deposited by a thermal evaporator, with a 50 μm diameter and the thickness was controlled by a thickness monitor. The phase formation and crystallinity for the depth information were monitored using GI-WAXD with $\lambda = 0.620831$ Å. The thickness of the PMO (4 nm)/BTO (4.3 nm)/CMO (3 nm)/Si (100) multilayer structure film was measured by XRR (Rigaku SmartLab). GI-WAXD measurements were taken with the PLS-II 9A U-SAX beamline at the Pohang Accelerator Laboratory (PAL) in Korea. The X-rays coming from the in-vacuum undulator (IVU) were monochromated using Si(111) double crystals and focused at the detector position using a K−B type mirror. GI-WAXD patterns were recorded with a 2D CCD detector (Rayonix SX165) and the X-ray irradiation time was 2−120 s depending on the saturation level of detector. Diffraction angles were calibrated by a precalibrated sucrose (Monoclinic, $P2_1$, $a = 10.8631$ Å, $b = 8.7044$ Å, $c = 7.7624$ Å, $\beta = 102.938°$) and Pt (111) substrate. The sample-to-detector distance was 223.3 mm. The band structure of the reference samples as PMO, BTO and CMO on the $Pt(111)/Ti/SiO_2/Si$ substrate were investigated using photoelectron spectroscopy (PES) and O 1s NEXAFS in an ultrahigh vacuum chamber of the 4D beamline at PAL. Au foil was used as a reference material for the calibration of the incident beam energy. The resistive switching behavior of the films was measured using a two-probe system with an Agilent B1500A semiconductor device analyzer. All measurements were performed at room temperature.

3. RESULTS AND DISCUSSION

3.1. Structural Investigation of Multilayer FTJ Device.

From the set process of off-axis rf magnetron sputtering, each PMO, BTO, and CMO thin film was deposited at a thickness of 5 nm by an in situ process on chemically cleaned $Pt(111)/Ti/SiO_2/Si(100)$. The average thickness of each layer was found to be PMO 4 nm/BTO 4.3 nm/CMO 3 nm (on 10 × 10 mm area) from X-ray-reflectometry (XRR) analysis. The top Au electrode was deposited with a 50-μm diameter dot and 50 nm thickness. As shown in Figure 2, the complete $Au/Pr_{0.98}Ca_{0.02}MnO_3/BaTiO_3/Ca_{0.98}Pr_{0.02}MnO_3/Pt(111)$ sample with reference samples as PMO/Pt(111), BTO/Pt(111), and CMO/Pt(111) were investigated by the grazing incidence wide-angle X-ray diffraction (GI-WAXD) to monitor their crystal structure. Figure 2b shows the diffraction peaks of PMO/Pt(111), BTO/Pt(111), and CMO/Pt(111) reference

DOI: 10.1021/acsami.5b06117
ACS Appl. Mater. Interfaces 2015, 7, 22348−22354

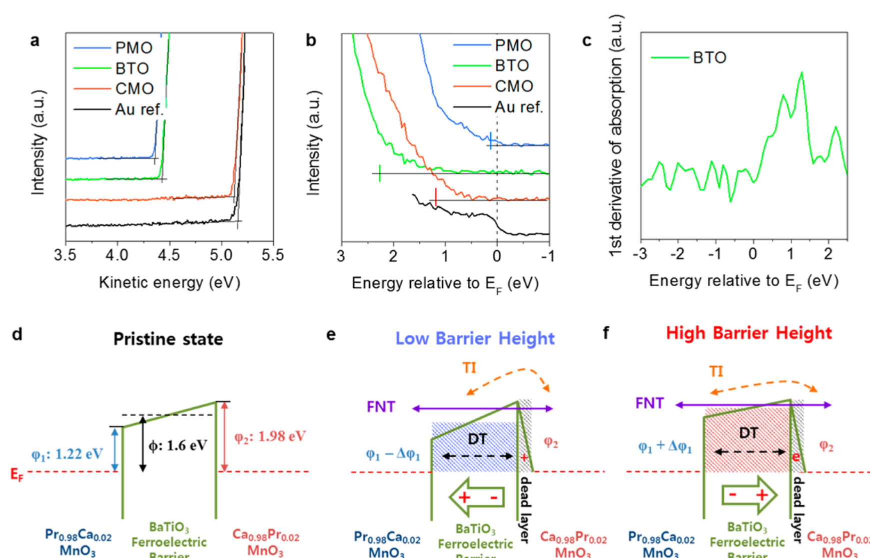

Figure 3. A schematic band diagram of the PMO (4 nm)/BTO (4.3 nm)/CMO (3 nm) structure. (a) Secondary cutoff, (b) valence band spectrum of PMO/Pt(111), BTO/Pt(111), CMO/Pt(111), and Au reference films. The E_{SE} spectrum is taken with a −5.0 V sample bias so that the sample inelastic cutoff can be distinguished and the incident beam energy and Fermi edge are defined by Au. (c) First derivation value of the O 1s NEXAFS of the BTO/Pt(111) reference film. Schematic band diagrams of PMO (4 nm)/BTO (4.3 nm)/CMO (3 nm): (d) pristine state, (e) low barrier height state, and (f) high barrier height state.

films that were vertical cut data of PMO/Pt(111), CMO/Pt(111) and *xy* cut data of BTO/Pt(111) because BTO film was grown to the (111) direction according to the Pt (111) surface (Supporting Information, Figure S3). PMO (130), BTO (111), and CMO (310) peaks were observed in the reference films. A 0.620831 Å wavelength was used in the GI-WAXD measurement. Therefore, from $\lambda = 2d \sin \theta$, PMO (130), CMO (310) plans were tilted approximately 7.6° to the Pt (111) surface. Each *d*-spacing was PMO (130): 2.319 Å, BTO (111): 2.315 Å, and CMO (310): 2.381 Å. The $BaTiO_3$ film was identified as the tetragonal phase (JCPDS: 05-0626). The stoichiometry of the reference films as $Pr_{0.98}Ca_{0.02}MnO_3$ and $Ca_{0.98}Pr_{0.02}MnO_3$ was investigated by X-ray photoelectron spectroscopy analysis and the atomic percent of substituted Pr and Ca cations was measured to be 0.5−0.6 atom % (Supporting Information, Figure S4). Figure 2 c, d and e show the diffraction peaks of the Au/PMO (130)/BTO (111)/CMO (310)/Pt(111) sample according to the incident angles 0.00001, 0.02, and 0.7°, which show the depth information. The phase formation of PMO (130)/BTO (111)/CMO (310)/Pt(111) was identified with the depth direction from the diffraction peak of the reference films. The corresponding angle to the PMO/BTO and BTO/CMO interface region was measured to investigate the interface condition. As shown in Figure 2f,g, the dead layer of the BTO ferroelectric film was observed at the BTO/CMO interface, while PMO/BTO has a clean interface. The diffraction peaks and the 2D image of Figure 2f,g show the BTO/CMO interface using angle variation from 0.26 to 0.04°. At the CMO top side, the beginning of the BTO film was observed with the end of the CMO film. BTO (111) (*d*-spacing 2.314 Å) appears with peak 'A', which has a smaller *d* spacing of 2.248 Å. The *d* spacing 2.248 Å of peak 'A' increased with a decrease (from bottom to top in the BTO film) of the incident angle and joined with the BTO (111) (*d*-spacing 2.314 Å) peak. Therefore, a dead layer exists on the bottom of the BTO film (BTO/CMO interface), which was generally induced by interdiffusion, lattice mismatch, and interface defect at the initial film growth.[17,31−34]

3.2. Band Structure of Au/PMO (130)/ BTO (111)/ CMO (310)/ Pt(111). As shown in Figure 3 a−c, the secondary cutoff, valence band, and O 1s near edge absorption fine structure (NEXAFS) of PMO/Pt(111), BTO/Pt(111), and CMO/Pt(111) reference films were measured to investigate the band structure of the Au/PMO/BTO/CMO/Pt(111) multilayer film. Au foil was used as a reference for the energy calibration and work function. Figure 3a,b show the spectrum of the secondary cutoff (E_{SE}) and Fermi energy (E_F) region using 95.1 eV photon energy. The E_{SE} spectrum was taken with a −5.0 V sample bias such that the sample inelastic cutoff could be distinguished, and the incident beam energy and Fermi edge were defined by Au. From $W_F = h\nu - (E_F - E_{SE})$, when the Au work function was set to 5.2 eV, the work function values of PMO, BTO, and CMO films were 4.40, 4.46, and 5.16 eV, respectively. The PMO shows a smaller work function value (approximately 0.76 eV) than CMO due to the occupation of the Mn 3d e^1_g band. From the valence band spectrum of Figure 3b, the distances of the valence band maximum (VBM) of PMO, BTO, and CMO from the Fermi level were 0.12, 2.26, and 1.18 eV, respectively. Figure 3c is the first derivation value of O 1s NEXAFS (the absorption calibrated by binding energy of O 1s core electron) that shows the conduction band minimum (CBM) from Fermi level. The distance from the Fermi level to CBM of BTO was approximately 1.28 eV. Therefore, in case of an ideal condition, a simplified schematic band diagram of the PMO/BTO/CMO structure could be depicted as Figure 3d from panels a−c. As shown in Figure 3d, a trapezoidal barrier was formed by the potential difference of approximately 0.76 eV for both sides (PMO, 4.40 eV; CMO, 5.16 eV), and the potential barrier heights of φ_1 and φ_2 were 1.22 and 1.98 eV, respectively. If interfacial bonding states of PMO/BTO and BTO/CMO were considered as $Mn^{3+}-O^{2-}-Ti^{3+}$ and $Ti^{3+}-O^{2-}-Mn^{4+}$ (electronegativity of Ti and Mn as 1.54 and 1.55), larger dipole could be formed at the BTO/CMO interface than the PMO/BTO interface. The interfacial bond could reduce a potential barrier height and the displacement of Ti^{3+} ion in BTO lattice could also change

DOI: 10.1021/acsami.5b06117
ACS Appl. Mater. Interfaces 2015, 7, 22348−22354

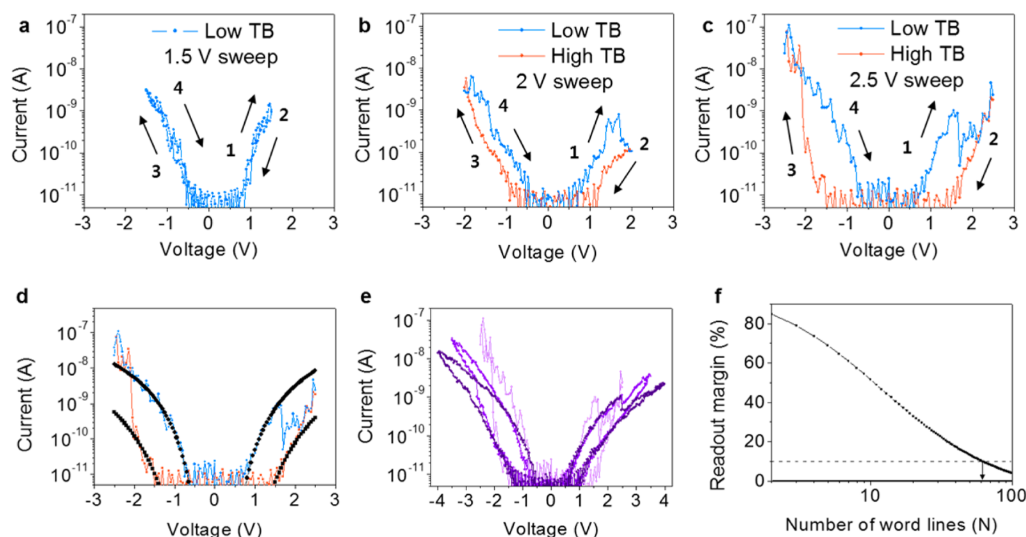

Figure 4. Memristive effect of the Au/PMO (4 nm)/BTO (4.3 nm)/CMO (3 nm)/Pt(111) structure. $I-V$ characteristics using (a) 1.5, (b) 2, and (c) 2.5 V sweeps. (d) Fitted $I-V$ curve with J_{FNT} based on eq (2) of Supporting Information (The parameters were d = 4.3 nm, $m_{e,ox} = m_e$, ε_{ifl} = 10, A** = 10^6 Am^{2-}K^{-2}, and T = 300 K). (e) The variation of $I-V$ characteristics due to thickness variation in a sample. (f) Readout margin as a function of N, the linear size of the simulated CPA, using the observed nonlinearity parameters.

the potential barrier from an ideal condition.[35−39] Therefore, the mean potential barrier height ϕ (($\varphi_1 + \varphi_2$)/2) was 1.6 eV. In the PMO side, a larger Thomas−Fermi screening length than the CMO side was expected via a strongly localized carrier. In addition, the Thomas−Fermi screening length with $\Delta\varphi_2$ in the CMO side could be reduced due to the screen effect of the dead layer at the bottom side of BTO. As observed in Figure 2, the dead layer has been widely observed in thin film capacitors of perovskite structure which degrades capacitance including ferroelectricity.[33,34] The ferroelectrically dead region of the bottom side of BTO could degrade the polarization at the bottom side of BTO which reduces the Thomas−Fermi screening length in CMO.[33,34,40−42] Therefore, in this case, the applied negative bias to the Au top electrode induces the polarization up state with a low mean barrier height as shown in Figure 3e and a positive bias induces the polarization down state with a high mean barrier height. On the basis of eq S3 (Supporting Information), when we consider the diameter (50 μm) of the Au electrode, the mean barrier height should be larger than 1 eV to minimize the sneak current in the low voltage region. Therefore, the FTJ as Au/PMO/BTO/CMO/Pt(111) of Figure 3d could be expected to show a suitable mean barrier height with an $I-V$ curve for the CPA structure. In addition, the applied electric field to the BTO layer will be smaller due to their serial contact with a high resistance oxide electrode as the PMO/BTO/CMO structure rather than direct contact with a metal electrode that would increase the starting voltage of FNT.

3.3. Memristive Characteristic and Application for CPA Structure. Figure 4a−c shows the $I-V$ curve of the 1.5, 2, and 2.5 V sweeps that was started at the LRS. The Au/PMO/BTO/CMO/Pt(111) structure shows resistive switching with a very high resistance. As shown in the $I-V$ curves, the current of the low voltage region, which induces a sneak current in the CPA structure, was effectively blocked and it could achieve resistive switching at a low current level. For a mean potential barrier height ϕ, the $I-V$ curve was fitted based on eq S2 (Supporting Information), in which J_{FNT} was a function of the barrier height and electric field. We could not determine the effective electric field that received the BTO layer in the Au/PMO/BTO/CMO/Pt(111) structure. The simulated curve based on the equation was designed for metal/insulator/metal condition while PMO and CMO layers have also resistance in the Au/PMO/BTO/CMO/Pt multilayer system as shown in Figure S2 (Supporting Information). Therefore, measured $I-V$ characteristic of Au/PMO/BTO/CMO/Pt(111) structure showed lower current level than the calculated $I-V$ curve while the shape and slope of measured $I-V$ curve were fitted well with the calculated $I-V$ curve. Therefore, Au/PMO/BTO/CMO/Pt was assumed to be a serial contact resistor and arbitrary resistance (d value set to 4.3 nm) was applied. As shown in Figure 4d, the measured $I-V$ curve fit well with a J_{FNT} curve and it showed asymmetric $I-V$ curve. When the current passed from top to bottom, the ϕ_L (barrier height in LRS) and ϕ_H (barrier height in HRS) values were fitted to 1.15 and 2.15 eV, respectively. In the reverse case (the current pass from bottom to top), the barrier height values were ϕ_L = 1.35 eV and ϕ_H = 2.20 eV, and $\Delta\phi$ was approximately 1 eV. This slightly asymmetric $I-V$ behavior originated from the trapezoidal barrier ($\varphi_1 < \varphi_2$) with asymmetric semiconductor electrodes as shown in Figure 3e,f. As shown in the $I-V$ curves of Figure 4a−c, the asymmetry of LRS larger than HRS which could be confirmed from the $I-V$ curve fitting such as ϕ_L = 1.35 eV (under positive), 1.15 eV (under negative) and ϕ_H = 2.20 eV (under positive), 2.15 eV (under negative). The ferroelectric film was investigated using by piezoresponse force microscopy measurement with BTO/CMO/Pt reference sample (Figure S5, Supporting Information). Figure 4e shows three different $I-V$ characteristics that were taken from the number of Au dots, which show a decrease in the curve slope. The sample had thickness variation from off-axis sputtering deposition (the side region was thicker than the center region in one sample). The decrease of the curve slope was induced by the reduced effective electric field in the thicker barrier. Therefore, a thicker barrier was advantageous for the CPA structure that shows the possibility of higher nonlinearity. From the observed values of nonlinearity in Figure 4d, using Kirchhoff circuit analysis, the readout margin of a CPA was simulated with N word lines, as

DOI: 10.1021/acsami.5b06117
ACS Appl. Mater. Interfaces 2015, 7, 22348−22354

shown in Figure 4f. Figure 1a shows the worst condition in the cross-point array circuit ($N \times N$) with the selected HRS cell surrounded by unselected LRS cells. In this case, the sneak current was maximized and the readout margin was minimized. When we read the selected cell (red cell), the sneak current was induced through unselected LRS cells (green cell). The selected resistor and sneak path resistors were connected as a parallel series and increasing the number of the N increases the sneak current. The number of word lines N in a cross-point array circuit can be simulated by the Kirchhoff equation (for more details see Section D in Supporting Information).[8,43,44] The simulated results based on the nonlinear $I-V$ curve in Figure 4d are shown in Figure 4f. At a readout margin of 10%, the possible number of word lines was 63 which value can fabricate 496 byte in one unit CPA cell. Consequently, the FTJ of the Au/PMO/BTO/CMO/Pt(111) structure achieved reduced sneak current in the reading process and minimized the voltage drop from operating in the low current level.

4. CONCLUSION

This study interpreted the resistive switching characteristic of PMO/BTO/CMO device based on simplified electrostatic model and calculated $I-V$ curve fitting. The change of potential barrier height could be affected by not only asymmetric Thomas−Fermi screening effect but also other factors such as the change of interfacial bonding state, interface dead layer, and electrochemical migration in real system. Nevertheless, the classical model was useful to approximate the observed memristive phenomena of multilayer FTJ system of complex oxide. From the electrostatic model and multilayer FTJ system, we demonstrated a suitable application of FTJ as a memristor of the CPA structure. To date, the CPA structure using a redox-based memristor was restricted to minimize the operating current level that induces a voltage drop in the operating process. With a polycrystalline FTJ as a Au/small doped p-type PMO (4 nm)/BTO (4.3 nm)/small doped n-type CMO (3 nm)/Pt(111) structure, which has a higher and thicker potential barrier, a good memristive effect for the CPA structure with a high nonlinear $I-V$ curve with minimized voltage drop (operating in a low current level) could be obtained by ΔJ_{FNT} by effectively blocking J_{DT} and J_{TI}. Consequently, the FTJ of this study demonstrated the reduced sneak current and the possibility of high nonlinearity.

■ ASSOCIATED CONTENT

Supporting Information

The Supporting Information is available free of charge on the ACS Publications website at DOI: 10.1021/acsami.5b06117.

> Carrier transport mechanisms in metal/insulator/metal structure; perovskite manganite family $Pr_{0.98}Ca_{0.02}MnO_3$ and $Ca_{0.98}Pr_{0.02}MnO_3$; GI-WAXD of $BaTiO_3$ /Pt (111) reference and the X-ray photoelectron spectroscopy; and simulation method for the number of N of cross point array.(PDF)

■ AUTHOR INFORMATION

Corresponding Author

* E-mail: hhpark@yonsei.ac.kr.

Notes

The authors declare no competing financial interest.

■ ACKNOWLEDGMENTS

This work was supported by the Industrial Strategic technology development program (10041926, Development of high-density plasma technologies for thin film deposition of nanoscale semiconductor and flexible display processing) funded by the Ministry of Knowledge Economy (MKE, Korea). The experiments at the PLS were supported in part by MSIP and POSTECH.

■ REFERENCES

(1) Garcia, V.; Bibes, M. Ferroelectric Tunnel Junctions for Information Storage and Processing. *Nat. Commun.* **2014**, *5*, 4289.

(2) Ramesh, R.; Spaldin, N. A. Multiferroics: Progress and Prospects in Thin Films. *Nat. Mater.* **2007**, *6*, 21−29.

(3) Wuttig, M. Phase-Change Materials: Towards a Universal Memory? *Nat. Mater.* **2005**, *4*, 265−266.

(4) Chappert, C.; Fert, A.; Van Dau, F. N. The Emergence of Spin Electronics in Data Storage. *Nat. Mater.* **2007**, *6*, 813−823.

(5) Waser, R.; Dittmann, R.; Staikov, G.; Szot, K. Redox-Based Resistive Switching Memories - Nanoionic Mechanisms, Prospects, and Challenges. *Adv. Mater.* **2009**, *21*, 2632−2663.

(6) Rozenberg, M. J. Resistive Switching. *Scholarpedia* **2011**, *6*, 11414.

(7) Szot, K.; Speier, W.; Bihlmayer, G.; Waser, R. Switching the Electrical Resistance of Individual Dislocations in Single-Crystalline $SrTiO_3$. *Nat. Mater.* **2006**, *5*, 312−320.

(8) Linn, E.; Rosezin, R.; Kügeler, C.; Waser, R. Complementary Resistive Switches for Passive Nanocrossbar Memories. *Nat. Mater.* **2010**, *9*, 403−406.

(9) Lee, M.-J.; Lee, C. B.; Lee, D.; Lee, S. R.; Chang, M.; Hur, J. H.; Kim, Y.-B.; Kim, C.-J.; Seo, D. H.; Seo, S.; Chung, U.-I.; Yoo, I.-K.; Kim, K. A Fast, High-Endurance and Scalable Non-Volatile Memory Device Made from Asymmetric Ta_2O_{5-x}/TaO_{2-x} Bilayer Structures. *Nat. Mater.* **2011**, *10*, 625−630.

(10) Yang, J. J.; Pickett, M. D.; Li, X.; Ohlberg, D. A. A.; Stewart, D. R.; Williams, R. S. Memristive Switching Mechanism for Metal/Oxide/Metal Nanodevices. *Nat. Nanotechnol.* **2008**, *3*, 429−433.

(11) Lee, W.; Park, J.; Kim, S.; Woo, J.; Shin, J.; Choi, G.; Park, S.; Lee, D.; Cha, E.; Lee, B. H.; Hwang, H. High Current Density and Nonlinearity Combination of Selection Device Based on $TaO_x/TiO_2/TaO_x$ Structure for One Selector-One Resistor Arrays. *ACS Nano* **2012**, *6*, 8166−8172.

(12) Yoon, J. H.; Song, S. J.; Yoo, I.-H.; Seok, J. Y.; Yoon, K. J.; Kwon, D. E.; Park, T. H.; Hwang, C. S. Highly Uniform, Electroforming-Free, and Self-Rectifying Resistive Memory in the $Pt/Ta_2O_5/HfO_{2-x}/TiN$ Structure. *Adv. Funct. Mater.* **2014**, *24*, 5086−5095.

(13) Pantel, D.; Alexe, M. Electroresistance Effects in Ferroelectric Tunnel Barriers. *Phys. Rev. B: Condens. Matter Mater. Phys.* **2010**, *82*, 134105.

(14) Gruverman, A.; Wu, D.; Lu, H.; wang, Y.; Jang, H. W.; Folkman, C. M.; Zhuravlev, M. Y.; Felker, D.; Rzchowski, M.; Eom, C.-B.; Tsymbal, E. Y. Tunneling Electroresistance Effect in Ferroelectric Tunnel Junctions at the Nanoscale. *Nano Lett.* **2009**, *9*, 3539−3543.

(15) Fowler, R. H.; Nordheim, L. Electron Emission in Intense Electric Fields. *Proc. R. Soc. London, Ser. A* **1928**, *119*, 173−181.

(16) Sze, S. M. *Physics of Semiconductor Devices*, 3rd ed. Wiley-Interscience: Hoboken, NJ, 2007.

(17) Kohlstedt, H.; Pertsev, N. A.; Rodriguez Contreras, J.; Waser, R. Theoretical Current-Voltage Characteristics of Ferroelectric Tunnel Junctions. *Phys. Rev. B: Condens. Matter Mater. Phys.* **2005**, *72*, 125341.

(18) Zhuravlev, M. Y.; Sabirianov, R. F.; Jaswal, S. S.; Tsymbal, E. Y. Giant Electroresistance in Ferroelectric Tunnel Junctions. *Phys. Rev. Lett.* **2005**, *94*, 246802.

(19) Chanthbouala, A.; Crassous, A.; Garcia, V.; Bouzehouane, K.; Fusil, S.; Moya, X.; Allibe, J.; Dlubak, B.; Grollier, J.; Xavier, S.; Deranlot, C.; Moshar, A.; Proksch, R.; Mathur, N. D.; Bibes, M.;

Barthélémy, A. Solid-State Memories Based on Ferroelectric Tunnel Junctions. *Nat. Nanotechnol.* **2011**, *7*, 101−104.

(20) Chanthbouala, A.; Garcia, V.; Cherifi, R. O.; Bouzehouane, K.; Fusil, S.; Moya, X.; Xavier, S.; Yamada, H.; Deranlot, C.; Mathur, N. D.; Bibes, M.; Barthélémy, A.; Grollier, J. A Ferroelectric Memristor. *Nat. Mater.* **2012**, *11*, 860−864.

(21) Soni, R.; Petraru, A.; Meuffels, P.; Vavra, O.; Ziegler, M.; Kim, S. K.; Jeong, D. S.; Pertsev, N. A.; Kohlstedt, H. Giant Electrode Effect on Tunneling Electroresistance in Ferroelectric Tunnel Junctions. *Nat. Commun.* **2014**, *5*, 5414.

(22) Pantel, D.; Goetze, S.; Hesse, D.; Alexe, M. Room-Temperature Ferroelectric Resistive Switching in Ultrathin $Pb(Zr_{0.2}Ti_{0.8})O_3$ Films. *ACS Nano* **2011**, *5*, 6032−6038.

(23) Dagotto, E. *Nanoscale Phase Separation and Colossal Magnetoresistance*; Springer-Verlag: Berlin Heidelberg, 2003.

(24) Salamon, M. B.; Jaime, M. The Physics of Manganites: Structure and Transport. *Rev. Mod. Phys.* **2001**, *73*, 583−628.

(25) Wadati, H.; Maniwa, A.; Chikamatsu, A.; Ohkubo, I.; Kumigashira, H.; Oshima, M.; Fujimori, A.; Lippmaa, M.; Kawasaki, M.; Koinuma, H. In Situ Photoemission Study of $Pr_{1-x}Ca_xMnO_3$ Epitaxial Thin Films with Suppressed Charge Fluctuations. *Phys. Rev. Lett.* **2008**, *100*, 026402.

(26) Satpathy, S.; Popović, Z. S.; Vukajlović, F. R. Electronic Structure of the Perovskite Oxides: $La_{1-x}Ca_xMnO_3$. *Phys. Rev. Lett.* **1996**, *76*, 960−963.

(27) Raabe, S.; Mierwaldt, D.; Ciston, J.; Uijttewaal, M.; Stein, H.; Hoffmann, J.; Zhu, Y.; Blöchl, P.; Jooss, C. In Situ Electrochemical Electron Microscopy Study of Oxygen Evolution Activity of Doped Manganite Perovskites. *Adv. Funct. Mater.* **2012**, *22*, 3378−3388.

(28) Jooss, Ch.; Wu, L.; Beetz, T.; Klie, R. F.; Beleggia, M.; Schofield, M. A.; Schramm, S.; Hoffmann, J.; Zhu, Y. Polaron Melting and Ordering as Key Mechanisms for Colossal Resistance Effects in Manganites. *Proc. Natl. Acad. Sci. U. S. A.* **2007**, *104*, 13597−13602.

(29) Jooss, Ch.; Hoffmann, J.; Fladerer, J.; Ehrhardt, M.; Beetz, T.; Wu, L.; Zhu, Y. Electric Pulse Induced Resistance Change Effect in Manganites due to Polaron Localization at the Metal-Oxide Interfacial Region. *Phys. Rev. B: Condens. Matter Mater. Phys.* **2008**, *77*, 132409.

(30) Lee, H. S.; Choi, S. G.; Park, H.-H.; Rozenberg, M. J. A New Route to the Mott-Hubbard Metal-Insulator Transition: Strong Correlations Effects in $Pr_{0.7}Ca_{0.3}MnO_3$. *Sci. Rep.* **2013**, *3*, 1704.

(31) Stengel, M.; Spaldin, N. A. Origin of the Dielectric Dead Layer in Nanoscale Capacitors. *Nature* **2006**, *443*, 679−682.

(32) Sinnamon, L. J.; Bowman, R. M.; Gregg, J. M. Investigation of Dead-Layer Thickness in $SrRuO_3/Ba_{0.5}Sr_{0.5}TiO_3$/Au Thin-Film Capacitors. *Appl. Phys. Lett.* **2001**, *78*, 1724.

(33) Zhou, C.; Newns, D. M. Intrinsic Dead Layer Effect and the Performance of Ferroelectric Thin Film Capacitors. *J. Appl. Phys.* **1997**, *82*, 3081.

(34) Sun, P.; Wu, Y.-Z.; Cai, T.-Y.; Ju, S. Effects of Ferroelectric Dead Layer on the Electron Transport in Ferroelectric Tunneling Junctions. *Appl. Phys. Lett.* **2011**, *99*, 052901.

(35) Peressi, M.; Binggeli, N.; Baldereschi, A. Band Engineering at Interfaces: Theory and Numerical Experiments. *J. Phys. D: Appl. Phys.* **1998**, *31*, 1273−1299.

(36) Liu, C.-T.; Zheng, Y.; Wang, B.; Chen, W.-J. Prediction of Ferroelectric Stability and Magnetoelectric Effect of Asymmetric Multiferroic Tunnel Junctions. *Appl. Phys. Lett.* **2013**, *102*, 152906.

(37) Chen, W.-J.; Zheng, Y.; Luo, X.; Wang, B.; Woo, C.-H. *Ab Initio* Study on the Size Effect of Symmetric and Asymmetric Ferroelectric Tunnel Junctions: A Comprehensive Picture with Regard to the Details of Electrode/Ferroelectric Interfaces. *J. Appl. Phys.* **2013**, *114*, 064105.

(38) Umeno, Y.; Albina, J.-M.; Meyer, B.; Elsässer, C. Ab Initio Calculations of Ferroelectric Instability in $PbTiO_3$ Capacitors with Symmetric and Asymmetric Electrode Layers. *Phys. Rev. B: Condens. Matter Mater. Phys.* **2009**, *80*, 205122.

(39) Minohara, M.; Yasuhara, R.; Kumigashira, H.; Oshima, M. Termination Layer Dependence of Schottky Barrier Height for $La_{0.6}Sr_{0.4}MnO_3$ /Nb:$SrTiO_3$ Heterojunctions. *Phys. Rev. B: Condens. Matter Mater. Phys.* **2010**, *81*, 235322.

(40) Bilc, D. I.; Novaes, F. D.; Íñiguez, J.; Ordejón, P.; Ghosez, P. Electroresistance Effect in Ferroelectric Tunnel Junctions with Symmetric Electrodes. *ACS Nano* **2012**, *6*, 1473−1478.

(41) Sun, P.; Wu, Y.-Z.; Zhu, S.-H.; Cai, T.-Y.; Ju, S. Interfacial Dead Layer Effects on Current-Voltage Characteristics in Asymmetric Ferroelectric Tunnel Junctions. *J. Appl. Phys.* **2013**, *113*, 174101.

(42) Liu, Y.; Lou, X.; Bibes, M.; Dkhil, B. Effect of a Built-In Electric Field in Asymmetric Ferroelectric Tunnel Junctions. *Phys. Rev. B: Condens. Matter Mater. Phys.* **2013**, *88*, 024106.

(43) Amsinck, C. J.; Di Spigna, N. H.; Nackashi, D. P.; Franzon, P. D. Scaling Constraints in Nanoelectronic Random-Access Memories. *Nanotechnology* **2005**, *16*, 2251−2260.

(44) Huang, J.-J.; Tseng, Y.-M.; Hsu, C.-W.; Hou, T.-H. Bipolar Nonlinear Selector for 1S1R Crossbar Array Applications. *IEEE Electron Device Lett.* **2011**, *32*, 1427−1429.

DOI: 10.1021/acsami.5b06117
ACS Appl. Mater. Interfaces 2015, 7, 22348−22354